

## Electrocatalysis

## A Cobalt@Cucurbit[5]uril Complex as a Highly Efficient Supramolecular Catalyst for Electrochemical and Photoelectrochemical Water Splitting

Fusheng Li<sup>+</sup>,\* Hao Yang<sup>+</sup>, Qiming Zhuo, Dinghua Zhou, Xiujuan Wu, Peili Zhang, Zhaoyang Yao, and Licheng Sun\*

**Abstract:** A host–guest complex self-assembled through  $\text{Co}^{2+}$  and cucurbit[5]uril (Co@CB[5]) is used as a supramolecular catalyst on the surface of metal oxides including porous indium tin oxide (ITO) and porous  $\text{BiVO}_4$  for efficient electrochemical and photoelectrochemical water oxidation. When immobilized on ITO, Co@CB[5] exhibited a turnover frequency (TOF) of  $9.9 \text{ s}^{-1}$  at overpotential  $\eta = 550 \text{ mV}$  in a pH 9.2 borate buffer. Meanwhile, when Co@CB[5] complex was immobilized onto the surface of  $\text{BiVO}_4$  semiconductor, the assembled Co@CB[5]/ $\text{BiVO}_4$  photoanode exhibited a low onset potential of  $0.15 \text{ V}$  (vs. RHE) and a high photocurrent of  $4.8 \text{ mA cm}^{-2}$  at  $1.23 \text{ V}$  (vs. RHE) under  $100 \text{ mW cm}^{-2}$  (AM 1.5) light illumination. Kinetic studies confirmed that Co@CB[5] acts as a supramolecular water oxidation catalyst, and can effectively accelerate interfacial charge transfer between  $\text{BiVO}_4$  and electrolyte. Surface charge recombination of  $\text{BiVO}_4$  can be also significantly suppressed by Co@CB[5].

## Introduction

Photoelectrochemical (PEC) water splitting is a promising strategy for converting solar energy into renewable fuels, such as hydrogen,<sup>[1]</sup> however, efficient catalytic water oxidation to provide protons for hydrogen production is considered to be a key challenge and one of the major obstacles for overall water splitting.<sup>[2]</sup> The sluggish multi-electron and multi-proton processes involved in the water oxidation reaction made many semiconductors having a low catalytic activity towards the oxygen evolution reaction (OER). Thus, it is well accepted that semiconductors should be integrated with water oxidation catalysts to achieve efficient solar water splitting.<sup>[3]</sup>

Recent studies have reported considerable improvements in the OER catalyzed by non-precious metal-based catalysts such as cobalt, iron and nickel in the form of oxide, hydroxide

and alloy with activity and stability benchmarks surpassing those of  $\text{RuO}_2$  and  $\text{IrO}_2$  under alkaline conditions.<sup>[4]</sup> Bismuth vanadate ( $\text{BiVO}_4$ ) showed great prospect as a photoanode material to be coupled with catalysts for OER, due to its appropriate band structure.<sup>[5]</sup>  $\text{BiVO}_4$  has been coupled with various OER material catalysts, such as  $\text{Co}_3\text{O}_4$ ,<sup>[6]</sup>  $\text{FeOOH}/\text{NiOOH}$ ,<sup>[7]</sup>  $\text{FeOOH}$ ,<sup>[8]</sup>  $\text{CoPi}$ ,<sup>[9]</sup>  $\text{NiBi}$ <sup>[10]</sup> and  $\text{NiB}$  alloy.<sup>[11]</sup> However, these heterogeneous catalysts for OER on the electrode surface are generally prepared through hydrothermal, electrodeposition or photo-electrodeposition methods. In such processes, the thickness of the catalyst film has to be carefully controlled because it considerably influences the light absorption and the charge transport, therefore, ultra-thin layers of catalysts are beneficial for efficient catalyst-semiconductor hybrid photoanodes.<sup>[2,8]</sup> Apart from heterogeneous OER catalysts coupled with semiconductors, molecular catalysts have also attracted great attention owing to their high activity, structural diversity, and facility in mechanistic studies.<sup>[12,13]</sup> However, few efforts have been made to apply host–guest supramolecular complexes as molecular catalysts for semiconductor-based photoanodes.

Cucurbituril (CB[n]) is a kind of macrocyclic host compounds, which can readily coordinate with metal cations as carbonyl groups directed towards the cavity of its cyclic structure. Strong complexes can be formed with cations by ion-dipole interactions.<sup>[14,15]</sup> Furthermore, CB[n] can be anchored or physisorbed onto the surface of metal oxides ( $\text{MO}_x$ ),<sup>[16,17]</sup> which indicates that the host–guest complexes based a CB[n] and a metal cation could be immobilized onto the surface of a metal oxide-based semiconductor through the remaining carbonyl groups. In the CB[n] family, CB[5] and CB[7] are moderately soluble in water (with concentration of 20–30 mM),<sup>[18]</sup> which is favorable for the construction of water splitting devices. In the present work, we selected CB[5] and

[\*] Dr. F. Li,<sup>[+]</sup> Q. Zhuo, D. Zhou, Dr. X. Wu, Dr. P. Zhang, Prof. Dr. L. Sun State Key Laboratory of Fine Chemicals, Institute of Artificial Photosynthesis, DUT-KTH Joint Education and Research Centre on Molecular Devices, Dalian University of Technology 116024 Dalian (China)  
E-mail: fusheng@dut.edu.cn  
lichengs@kth.se

H. Yang,<sup>[+]</sup> Dr. Z. Yao, Prof. Dr. L. Sun Department of Chemistry, School of Engineering Sciences in Chemistry, Biotechnology and Health KTH Royal Institute of Technology, 10044 Stockholm (Sweden)

Prof. Dr. L. Sun Center of Artificial Photosynthesis for Solar Fuels, School of Science Westlake University, 310024 Hangzhou (China)

[\*] These authors contributed equally to this work.

Supporting information and the ORCID identification number(s) for the author(s) of this article can be found under: <https://doi.org/10.1002/anie.202011069>.

© 2020 The Authors. Angewandte Chemie International Edition published by Wiley-VCH GmbH. This is an open access article under the terms of the Creative Commons Attribution License, which permits use, distribution and reproduction in any medium, provided the original work is properly cited.

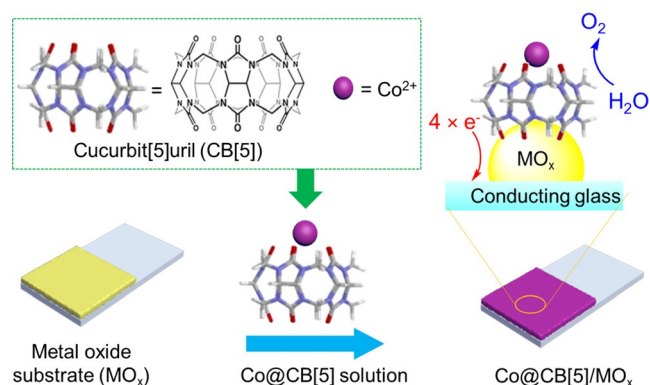
Co<sup>2+</sup> cation for the supramolecular assembly, and immobilized Co@CB[5] on the surface of metal oxides to study its activity for electrochemical and PEC water splitting. For the first time, we could demonstrate a host-guest complex Co@CB[5], which is applied to a porous ITO or BiVO<sub>4</sub> surface, achieving the electrochemical and PEC water oxidation performance comparable with that of state-of-the-art heterogeneous water oxidation catalysts, but with a much simpler preparation procedure. These new findings show the huge potential of host-guest supramolecular complexes as catalysts for efficient OER.

## Results and Discussion

### Electrode Preparation and Characterization

The Co@CB[5] supramolecular complex was assembled on the porous indium tin oxide (ITO) and porous BiVO<sub>4</sub> substrates to evaluate the electrochemical-driven and PEC oxygen evolution activity of the proposed host-guest assembled devices, respectively. The porous ITO substrate was prepared by a doctor-blade method (see the Supporting Information for details). The BiVO<sub>4</sub> thin film was prepared by modifying a method reported by Choi and co-workers.<sup>[19]</sup> This porous BiVO<sub>4</sub> film has the advantages of improving electron-hole separation and suppressing bulk carrier recombination,<sup>[12]</sup> while also providing a large specific surface area for loading the Co@CB[5] onto the electrode surface. The porous ITO substrate was composed of octahedron shape particles as indicated by scanning electron microscope (SEM) images (Figure S1a). A cross-sectional view of the film showed that the porous ITO layer had an average thickness of approximately 1.3 μm (Figure S1b). The porous BiVO<sub>4</sub> film was composed of worm-like particles as indicated by SEM images (Figure S2a). A cross-sectional view of the film showed that the BiVO<sub>4</sub> layer had an average thickness of approximate 1 μm (Figure S2b). Energy dispersive spectroscopy (EDS) mapping analysis was performed on a selected cross-sectional area to determine the elemental distribution (Figure S2c), which demonstrated a homogeneous distribution of Bi, V, and O elements in the film of the porous BiVO<sub>4</sub>.

The preparation of Co@CB[5]/ITO and Co@CB[5]/BiVO<sub>4</sub> electrodes was briefly illustrated in Scheme 1. First, a solution of Co@CB[5] host-guest complex (1.0 mM) was prepared by mixing CB[5] and Co(NO<sub>3</sub>)<sub>2</sub> in a molar ratio of 1:1. Mass-to-charge ratio (m/e) of 454.0879 corresponding to Co@CB[5] + H<sub>2</sub>O (m/e 454.0979) could be found by electrospray mass spectrometry (Figure S3). Then, the porous ITO and BiVO<sub>4</sub> substrates were immersed in the solution of Co@CB[5] for 30 min, after washing with deionized water, resulting in the generation of Co@CB[5]/ITO and Co@CB[5]/BiVO<sub>4</sub> electrodes, respectively. The attenuated total reflection infrared (ATR-IR) spectra of Co@CB[5]/ITO, CB[5]/ITO electrode and bare CB[5] powder were acquired using an infrared spectrometer with a resolution of 0.09 cm<sup>-1</sup> (Figure S4). Red-shifts of ca. 9 and ca. 3 cm<sup>-1</sup> were observed for the carbonyl portal of the CB[5] component on Co@CB[5]/ITO and CB[5]/ITO electrode compared to that of CB[5]



**Scheme 1.** The electrode preparation process by immobilizing Co@CB[5] on the surface of metal oxide substrates.

powder (1738 cm<sup>-1</sup>), respectively. A similar red-shift on the carbonyl portal of the CB[5] component on Co@CB[5]/BiVO<sub>4</sub> and CB[5]/BiVO<sub>4</sub> could also be observed (Figure S5). These ATR-IR spectra suggested strong interaction between CB[5], Co cations and porous MO<sub>x</sub> substrates,<sup>[20]</sup> and indicated that Co@CB[5] was immobilized on the surface of ITO and BiVO<sub>4</sub>.

A time-of-flight secondary ion mass spectrometry (TOF-SIMS) with Bi<sub>3</sub><sup>+</sup> as the primary ion source was further employed to detect the presence of Co@CB[5] on the surface of ITO and BiVO<sub>4</sub>. As shown in the SIMS images of Co@CB[5]/ITO and Co@CB[5]/BiVO<sub>4</sub> (Figures S6 and S7), some related secondary ions assigned to cobalt combined with the fragments of CB[5] could be observed uniformly distributing on the surface of electrodes, indicating that Co@CB[5] was successfully immobilized on the surface of ITO and BiVO<sub>4</sub>.

The morphological features of Co@CB[5] functionalized electrodes were then investigated by SEM. As shown in Figures S8 and S9, no obvious morphological changes were observed after the immobilization of CB[5] and Co@CB[5] on the porous substrates, because the assembly process is a molecular level surface modification.

X-ray photoelectron spectroscopy (XPS) measurements were performed to analyze the molecular level surface composition and electronic states of the Co@CB[5] complex functionalized MO<sub>x</sub> substrates. The XPS survey spectra of Co@CB[5]/ITO, Co@CB[5]/BiVO<sub>4</sub> and reference electrodes are shown in Figures S10 and S11. In XPS high-resolution spectra of CB[5]/ITO and Co@CB[5]/BiVO<sub>4</sub> (Figures 1a,b, Figures 2a,b), when CB[5] was immobilized on the surface of MO<sub>x</sub>, the N 1s signal corresponding to the C-N of CB[5] at a binding energy of 400.15 eV can be observed, which indicated that CB[5] can be successfully immobilized on the surface of porous MO<sub>x</sub> substrates by the simple soaking method. When Co@CB[5] was immobilized on ITO or BiVO<sub>4</sub>, clear signal of Co 2p were observed at the binding energy around 781 eV, which did not appear for the bare substrates and neither for the CB[5]/MO<sub>x</sub> electrodes. Meanwhile, small offsets from the main signal of N 1s could be observed. The signal of Co 2p for Co@CB[5]/ITO was fitted by four peaks, namely Co 2p<sub>3/2</sub> at 781.0 eV, Co 2p<sub>3/2</sub> satellite at

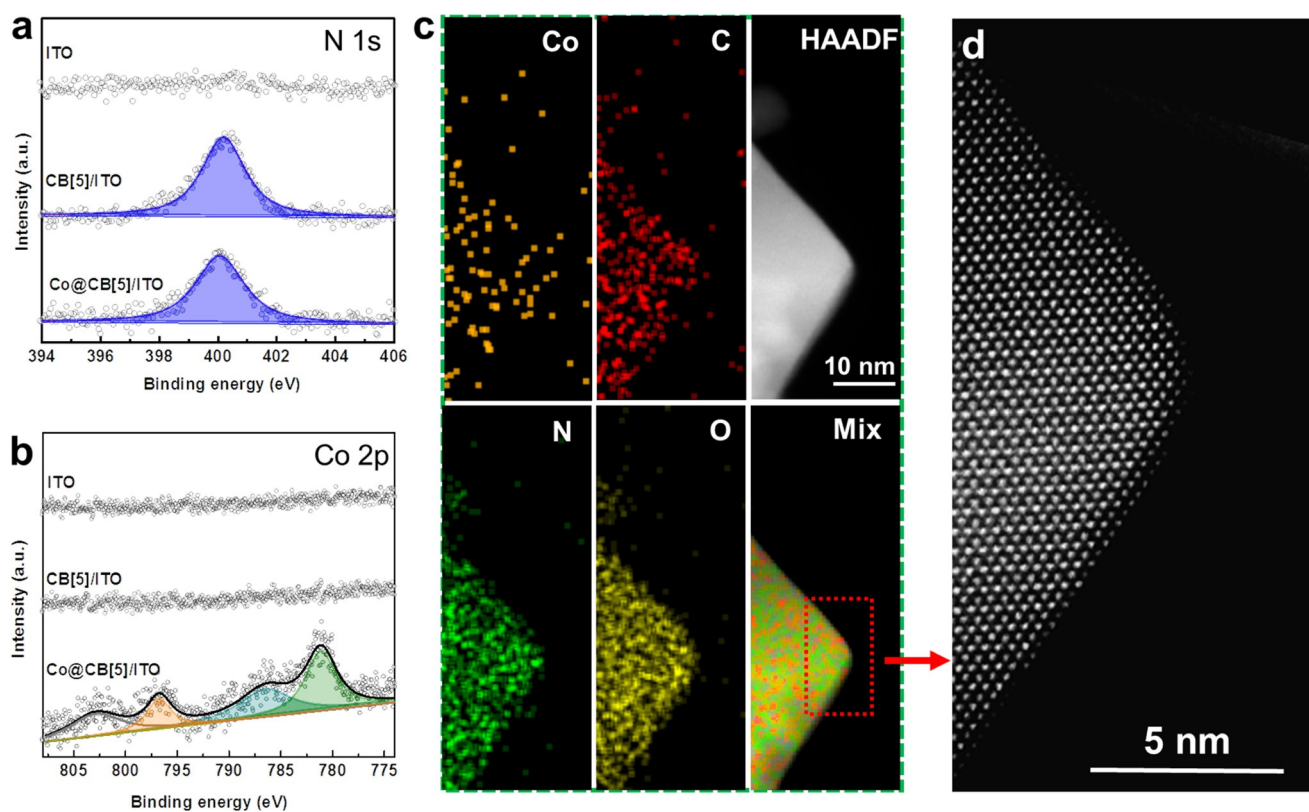


**Figure 1.** XPS spectra of ITO based electrodes in selected energy areas: a) N 1s, b) Co 2p. c) Energy-dispersive X-ray spectroscopy (EDS) maps of one Co@CB[5]/ITO particle. d) Atomic-resolution HAADF image of one Co@CB[5]/ITO particle in selected small area.

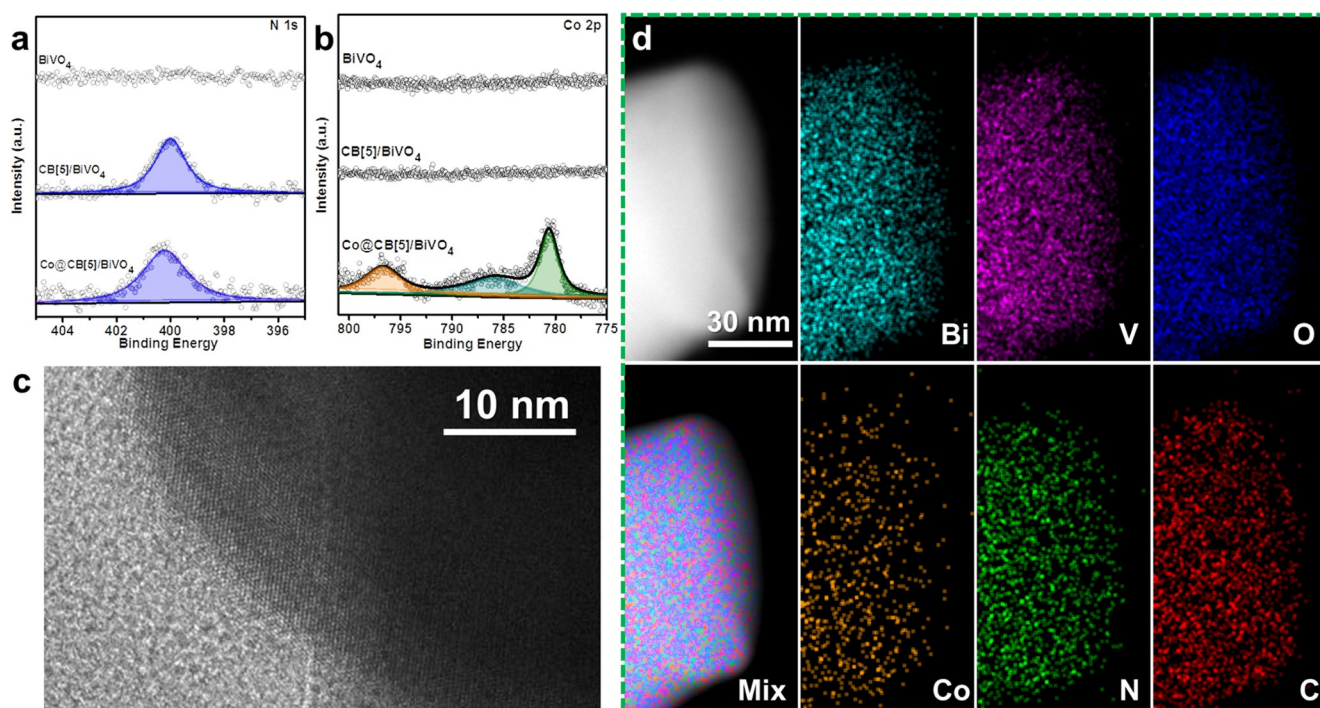


**Figure 2.** High-resolution XPS spectra of BiVO<sub>4</sub> based electrodes: a) N 1s and b) Co 2p. c) HRTEM image of the Co@CB[5]/BiVO<sub>4</sub> sample. d) HAADF-STEM images of Co@CB[5]/BiVO<sub>4</sub> electrode and corresponding elemental mappings.

786.3 eV, Co 2p<sub>1/2</sub> at 796.7 eV, and a Co 2p<sub>1/2</sub> satellite at 802.6 eV. The signal of Co 2p for Co@CB[5]/BiVO<sub>4</sub> was fitted into three peaks, Co 2p<sub>3/2</sub> at 780.7 eV, a Co 2p<sub>3/2</sub> satellite at 785.9 eV, and Co 2p<sub>1/2</sub> at 796.6 eV, (the Co 2p<sub>1/2</sub> satellite signal is not assigned here owing to its overlap with the BiVO<sub>4</sub> signal). Please note that the binding energies of Co 2p for Co@CB[5] complex were different from those of Co-based oxides or hydroxides,<sup>[21,22]</sup> indicating a molecular nature of the Co@CB[5] on MO<sub>x</sub> surfaces.

To further demonstrate that the Co@CB[5] is a molecular catalyst on MO<sub>x</sub>, the surface and morphology properties of the Co@CB[5]/ITO and Co@CB[5]/BiVO<sub>4</sub> samples were studied at atomic level by spherical aberration corrected transmission electron microscope (ACTEM). As revealed by high-angle annular dark-field (HAADF) images in Figure S12, the Co@CB[5]/ITO nano-particle exhibited octahedron shape with regular and clear edge. As shown in Figure 1c, Energy-dispersive X-ray spectroscopy (EDS) mapping images of Co@CB[5]/ITO showed the presence of Co, N and C on the surface of ITO nano-particle. Atomic-scale HAADF images in the Figure 1d revealed that there is no structural decomposition observed after the attachment of Co@CB[5] complex, meanwhile, no Co oxides or hydroxides could be observed on the terminations of ITO nano-particle after the immobilization of Co@CB[5] complex. This is in consistence with the phenomena of molecular anchoring of Co@CB[5] complex on ITO surface. As the element atomic mass of tin and indium in bulk ITO nanoparticle is far larger than that of cobalt, therefore, it is hard to pinpoint the single cobalt molecular complex absorbed on the surface of ITO by comparing the difference in atomic resolution HAADF images. Figures S13 and S14 have shown atomic-resolution TEM images and corresponding EDS mapping images of Co@CB[5]/ITO in different scales, which suggested that the cobalt components were uniformly distributed on the surface of ITO. In addition, according to the results of EDS analysis in selected area, the metal composition ratio of Co: In: Sn was estimated to be 1: 92: 7, this result was in accordance with the magnitude of surface mono-molecular layer distribution for Co components.<sup>[23]</sup>

The interface morphology of Co@CB[5]/BiVO<sub>4</sub> was characterized by high-resolution transmission electron microscope (HRTEM), as shown in Figure 2c, there were no obvious metal oxide films or nanoparticles covered on the surface of Co@CB[5]/BiVO<sub>4</sub> nanoparticle. Unfortunately, when high energy electron beam was focused on BiVO<sub>4</sub>, the surface of BiVO<sub>4</sub> was damaged, detailed structure information for the surface of Co@CB[5]/BiVO<sub>4</sub> could not be obtained by atomic resolution AC-STEM. HAADF-STEM and corresponding EDS mapping images of Co@CB[5]/BiVO<sub>4</sub> showed that elements of Co, N and C contents in the Co@CB[5] complex were uniformly distributed on the surface of the BiVO<sub>4</sub> nanoparticles (Figures 2d and S15). All above characterizations suggested that the Co@CB[5] on the surface of MO<sub>x</sub> is a molecular level immobilization.

### Electrochemically Driven OER Catalysis by the Co@CB[5] Complex

The OER performance of Co@CB[5]/ITO was first evaluated by linear sweep voltammetry (LSV). LSV measurements were performed at 25 °C in a standard three-electrode cell with 1.0 M borate buffer solution (pH 9.2) as the electrolyte. As shown in Figure 3a, the ITO substrate and CB[5]/ITO electrode were silent for OER. In contrast, the anodic current density curve of the Co@CB[5]/ITO electrode rose sharply beyond a low onset potential of 1.05 V vs. normal hydrogen electrode (NHE), followed by a dramatic increase at more positive potentials. A current density of 1.0 mA cm<sup>-2</sup> was achieved at  $\eta = 485$  mV. For comparison, Co/ITO electrode was also prepared by immersing ITO in 1.0 mM Co<sup>2+</sup> solution for 30 mins (the same immersion time as for Co@CB[5]/ITO). The Co/ITO electrode exhibited a much lower anodic current density than that of the Co@CB[5]/ITO electrode. Linear fitting of the Co@CB[5]/ITO electrode gives a Tafel slope of 59.5 mV dec<sup>-1</sup> (Figure 3b). The steady-state catalytic activities of Co@CB[5]/ITO were determined by chronopotentiometric measurements during electrolysis at constant current densities over 5 h (Figure 3c). The Co@CB[5]/ITO electrode required only 1.23 V and 1.29 V vs. NHE to achieve the current density of 1.0 mA cm<sup>-2</sup> and 2.5 mA cm<sup>-2</sup>, respectively. The overpotential requirement kept stable during the test, which indicated that the Co@CB[5]/ITO is stable for OER. The amount of electrochemically generated oxygen from the Co@CB[5]/ITO system was confirmed by gas chromatography (GC). When a total charge of 3.6 C passed through the electrode, 8.62  $\mu$ mol of O<sub>2</sub> was detected by GC, leading to a Faraday efficiency of 92.6% (Figure S16).

The effective coverage of Co<sup>2+</sup> on the surface of ITO was estimated as 4.54  $\times 10^{-9}$  mol cm<sup>-2</sup> according to the linear relationship between the peak current of Co<sup>2+/3+</sup> and the scan rate (Figure S17, Eq. S1 and Eq. S2), and the order of magnitude for such catalyst loading is consistent with that of molecules immobilized on the surface of porous metal oxide substrates.<sup>[24]</sup> This total loading amount of Co<sup>2+</sup> was further confirmed by inductively coupled plasma optical emission spectrometer (ICP-OES). The total Co<sup>2+</sup> loading amount is 4.98  $\times 10^{-9}$  mol cm<sup>-2</sup>, which was slightly larger than the redox active Co<sup>2+</sup>. The turn over frequencies (TOFs) of Co@CB[5]/ITO based on the Co<sup>2+</sup> loading (redox active) current densities vs. various overpotentials were calculated based on LSV data (operated in a low scan rate of 10 mV s<sup>-1</sup>) and Eq. S3.<sup>[25]</sup> The logarithm of the TOFs varied linearly on the applied overpotentials from 460 to 550 mV, as shown in Figure 3d. A TOF of 0.3 s<sup>-1</sup> was achieved at  $\eta = 460$  mV, which reached 9.9 s<sup>-1</sup> at  $\eta = 550$  mV. Table S1 lists the performance of Co@CB[5]/ITO in the current work and previously reported anodes for electrocatalytic water oxidation, including molecular and inorganic material catalysts immobilized on conducting glass. This comparison shows that the Co@CB[5]/ITO electrode is one of the best OER anodes in terms of overpotential, current density, and TOF.

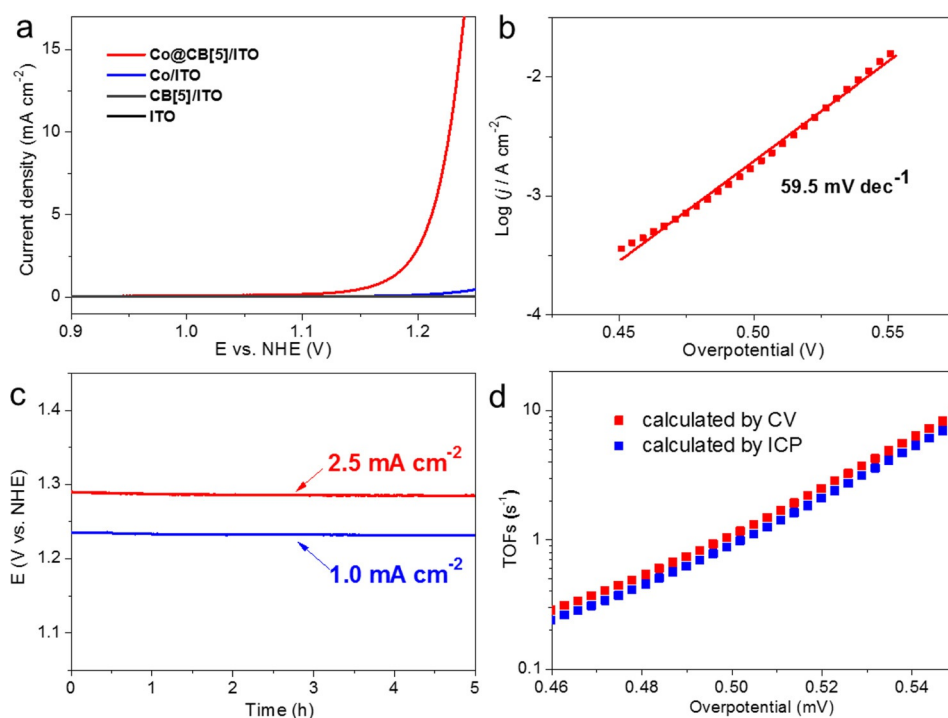


**Figure 3.** a) The LSV measurements of Co@CB[5]/ITO and comparison electrodes in 1.0 M borate buffer (pH 9.2) at a scan rate of  $50 \text{ mV s}^{-1}$  with *iR* compensation. b) Tafel plots of Co@CB[5]/ITO. c) Chronopotentiometric measurement of OER at current density of 1.0 and  $2.5 \text{ mA cm}^{-2}$  for 5 h without *iR* compensation. d) TOFs of Co@CB[5]/ITO based on the  $\text{Co}^{2+}$  loading (calculated according to electrochemical measurement and ICP-OES) and current densities vs. various overpotentials.

#### Photo-electrochemical Water Oxidation by Co@CB[5]/BiVO<sub>4</sub>

The PEC water oxidation performance of Co@CB[5]/BiVO<sub>4</sub> photoanode was measured by linear sweep voltammetry (LSV) with a scan rate of  $10 \text{ mV s}^{-1}$ . The absorption spectrum of BiVO<sub>4</sub> did not change after Co@CB[5] was immobilized on the surface of BiVO<sub>4</sub> (Figure S18), hence, the band gap of BiVO<sub>4</sub> and Co@CB[5]/BiVO<sub>4</sub> were the same.

As shown in Figure 4a, the photocurrent density of the as-prepared BiVO<sub>4</sub> at 1.23 V vs. RHE was approximate  $1.8 \text{ mA cm}^{-2}$ . In the presence of sulfite as hole scavenger, the photocurrent density of BiVO<sub>4</sub> increased to  $5.4 \text{ mA cm}^{-2}$ . These results are comparable with previously reported values,<sup>[26]</sup> which suggested that the quality of BiVO<sub>4</sub> film in our work is reliable. When Co@CB[5] was immobilized on the surface of BiVO<sub>4</sub>, the photocurrent density of the Co@CB[5]/BiVO<sub>4</sub> electrode was measured to be  $4.8 \text{ mA cm}^{-2}$  at 1.23 V vs. RHE without the hole scavenger sulfite, which is much greater than that of unmodified BiVO<sub>4</sub>, CB[5]/BiVO<sub>4</sub> and Co/BiVO<sub>4</sub> electrodes. The CB[5]/BiVO<sub>4</sub> electrode exhibited an similar anodic photocurrent density curve than that of the pristine BiVO<sub>4</sub> electrode (Figure S19), indicating CB[5] itself can not affect the water oxidation of BiVO<sub>4</sub>. After immersing BiVO<sub>4</sub> in  $\text{Co}^{2+}$  solution for 30 minutes, the photocurrent density of Co/BiVO<sub>4</sub> electrode at 1.23 V vs. RHE increased to  $2.3 \text{ mA cm}^{-2}$ , which is much lower than that of the Co@CB[5]/BiVO<sub>4</sub> electrode ( $4.8 \text{ mA cm}^{-2}$ ). The applied bias photon to current efficiency (ABPE) was calculated from the corresponding LSV curve in Figure 4a according to Eq. S4. The maximum ABPE of BiVO<sub>4</sub> was 0.32% at 0.88 V vs. RHE.

However, the maximum ABPE of Co@CB[5]/BiVO<sub>4</sub> was 1.79% at 0.60 V vs. RHE (Figure 4b), which is 5.5 times as high as that of unmodified BiVO<sub>4</sub>. The incident photon to current efficiencies (IPCEs) of BiVO<sub>4</sub> and Co@CB[5]/BiVO<sub>4</sub> were measured and calculated according to Eq. S5. As shown in Figure 4c, the IPCE values of BiVO<sub>4</sub> and Co@CB[5]/BiVO<sub>4</sub> were approximate 35% and 88% at 420 nm (1.23 V vs. RHE), respectively. The values of the ABPE and IPCE demonstrated the high photon-to-O<sub>2</sub> conversion efficiency of the host-guest complex assembled Co@CB[5]/BiVO<sub>4</sub> photoanode. On the basis of these measurements, the photocurrent densities were  $4.85 \text{ mA cm}^{-2}$  at 1.23 V vs. RHE and  $2.9 \text{ mA cm}^{-2}$  at 0.6 V vs. RHE for Co@CB[5]/BiVO<sub>4</sub>, as estimated by integrating the IPCE curves over the AM 1.5G solar spectrum (Figure S20). These calculated values are in agreement with the measured data in Figure 4a ( $4.8 \text{ mA cm}^{-2}$  at 1.23 V and  $2.8 \text{ mA cm}^{-2}$  at 0.6 V).

Under chopped-light illumination, the bare BiVO<sub>4</sub> only generated a low photocurrent density less than  $0.25 \text{ mA cm}^{-2}$  at a constant applied potential of 0.6 V vs. RHE; however, the Co@CB[5]/BiVO<sub>4</sub> photoanode generated a photocurrent density of ca.  $2.4 \text{ mA cm}^{-2}$ , underlining the indispensable role of Co@CB[5] in water splitting (Figure 4d). During long-term photolysis at 0.6 V vs. RHE under continued visible-light irradiation, the magnitude of the photocurrent generated by Co@CB[5]/BiVO<sub>4</sub> slowly decreased from  $2.5$  to  $2.3 \text{ mA cm}^{-2}$  over 30 min (Figure S21). The photogenerated O<sub>2</sub> in the headspace was quantified by GC. Assuming a  $4e^-$  process for O<sub>2</sub> evolution, the number of electrons passing through the electrode agreed well with the amount of O<sub>2</sub> detected,

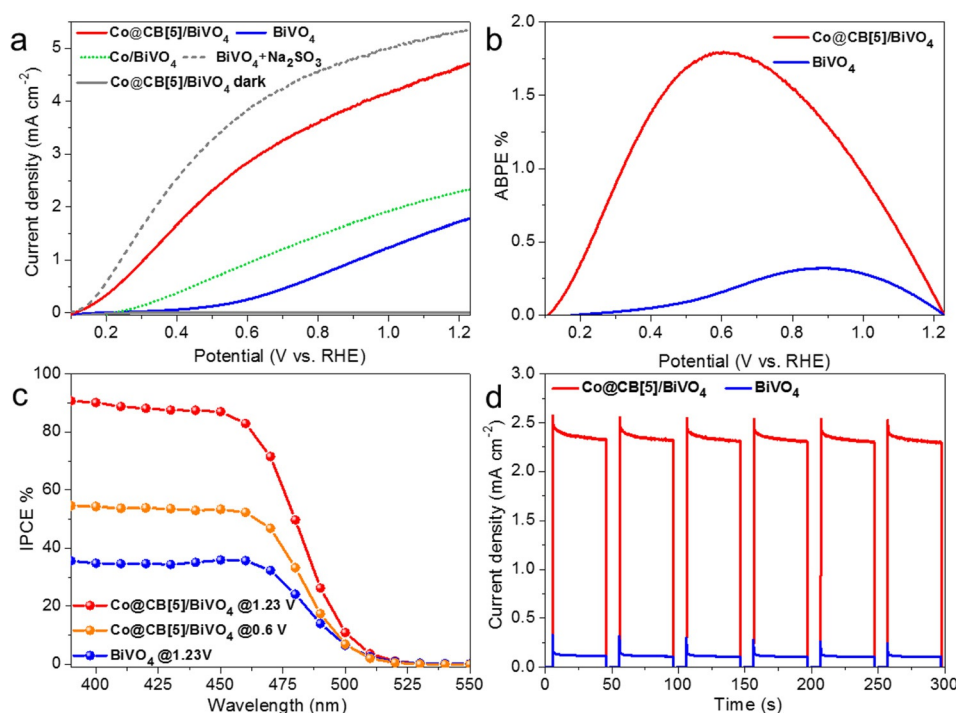


**Figure 4.** a) LSV curves of Co@CB[5]/BiVO<sub>4</sub>, Co/BiVO<sub>4</sub>, BiVO<sub>4</sub>, and BiVO<sub>4</sub> with the hole scavenger Na<sub>2</sub>SO<sub>3</sub> in 1 M borate buffer (scan rate, 10 mVs<sup>-1</sup>). b) ABPEs of Co@CB[5]/BiVO<sub>4</sub> and BiVO<sub>4</sub> calculated from LSV curves. c) IPCEs of Co@CB[5]/BiVO<sub>4</sub> at 1.23 V and 0.6 V vs. RHE, and BiVO<sub>4</sub> at 1.23 V vs. RHE. d) Light response of Co@CB[5]/BiVO<sub>4</sub> and BiVO<sub>4</sub> photoanodes under chopped irradiation at a constant bias of 0.6 V vs. RHE.

representing a Faradaic efficiency of 90.3% for Co@CB[5]/BiVO<sub>4</sub> photoanode (Figure S22).

The photocurrent density at 1.23 V vs. RHE and the maximum ABPE obtained from Co@CB[5]/BiVO<sub>4</sub> are compared to those previously reported systems and the results are shown in Table S2. The performance of Co@CB[5]/BiVO<sub>4</sub> exceeded those of many catalyst-modified undoped-BiVO<sub>4</sub> photoanodes in both parameters. The host-guest complex assembled Co@CB[5]/BiVO<sub>4</sub> photoanode can avoid complicated organic synthesis, and the high activity of Co@CB[5]/BiVO<sub>4</sub> holds potential for supramolecular catalysts capable of replacing state-of-the-art metal oxides and molecular catalysts.

#### Post-characterization of the Electrode after the OER Test

Post-characterization of the electrode after the OER test is necessary for further proof of reaction mechanism and the stability of the as-fabricated hybrid electrodes. As shown in ATR-IR spectra (Figure S23), Co@CB[5] maintained on the surface of electrodes after the OER test. As shown in Figures S24 and S25, the SEM images revealed that the Co@CB[5]/ITO and Co@CB[5]/BiVO<sub>4</sub> after OER test maintained a porous surface without significant changes. The composition and electronic states of the Co@CB[5]/ITO and Co@CB[5]/BiVO<sub>4</sub> samples after OER test were analyzed by XPS technique (Figures S26–S29). The binding energies of both N 1s and Co 2p for Co@CB[5]/ITO and Co@CB[5]/BiVO<sub>4</sub> were consistent with that of before OER test,

indicating that Co@CB[5] was stable for OER. The EDS elemental mapping images with different magnitudes in Figures S30a, S31 and S32 confirmed the uniform distribution of Co, N and C in Co@CB[5]/ITO following the OER tests. Figure S30b showed the atomic-resolution TEM images of tested Co@CB[5]/ITO particle. By further observing the edge of sample under greater magnification, a clear and well-ordered surface could be observed of tested Co@CB[5]/ITO, indicating that there was no other amorphous layer or heterojunction film formed to covered ITO nano-particle surface during the OER process (Figure S30c,d). In addition, according to the results of EDS analysis in selected area, the metal composition ratio of Co: In: Sn for tested Co@CB[5]/ITO particle was calculated to be 1: 91: 8, which was almost the same as the ratio of pristine Co@CB[5]/ITO. The EDS elemental mapping images with different magnitudes in Figure S33 and S34 confirmed the uniform distribution of Co, N and C in Co@CB[5]/BiVO<sub>4</sub> after the OER tests. Figure S35 showed the HRTEM images of the tested Co@CB[5]/BiVO<sub>4</sub> particles, there are no nanoparticles generated on the surface of Co@CB[5]/BiVO<sub>4</sub> during the OER process, indicating that Co@CB[5] was stable on the surface of BiVO<sub>4</sub> during the OER. By integrating the information obtained from the above characterizations, it can be convincingly concluded that Co@CB[5] maintains its supramolecular nature and is stable during the OER.

## Kinetic Studies of Co@CB[5] for Water Oxidation

To investigate the transfer of carriers in the PEC system constructed by this novel Co@CB[5] supramolecular catalyst, kinetic studies were carried out. With sodium sulfite ( $\text{Na}_2\text{SO}_3$ ) as a hole scavenger, extremely fast oxidation kinetics and negligible surface recombination were expected, as shown in Figure S36, the charge transfer efficiency ( $\eta_{\text{trans}}$ ) at the electrode-electrolyte interface was calculated according to Eq. S6 and the data from Figure 4a. Using this method, a superior  $\eta_{\text{trans}}$  of Co@CB[5]/BiVO<sub>4</sub> was achieved (88%), compared with that of bare BiVO<sub>4</sub> (33%) at 1.23 V vs. RHE. This result suggests that the Co@CB[5]/BiVO<sub>4</sub> electrode has more rapid water oxidation kinetics than the bare BiVO<sub>4</sub>.<sup>[27]</sup>

Electrochemical impedance spectroscopy (EIS) was performed to examine the charge transport phenomena in the bulk and at the surface of the electrodes. As shown in Figure 5a, semicircles for Co@CB[5]/BiVO<sub>4</sub> and BiVO<sub>4</sub> electrodes fitted well with Randles equivalent circuit model. Charge transport at the photoanode-electrolyte interface was estimated with the values for the charge-transfer resistance ( $R_{\text{ct}}$ ) obtained from the diameter of the semicircles. A smaller semicircle indicates better charge transfer of the corresponding photoanode at the interface. Notably, the Co@CB[5]/BiVO<sub>4</sub> electrode had a markedly smaller  $R_{\text{ct}}$  (96  $\Omega$ ) value than that of bare BiVO<sub>4</sub> (303  $\Omega$ ) under illumination at 0.6 V vs. RHE, illustrating a better ability to transfer holes at the electrode-electrolyte interface of Co@CB[5]/BiVO<sub>4</sub>, which was consistent with its high charge transfer efficiency ( $\eta_{\text{trans}}$ ).

The charge transfer efficiency depends on the rate of water oxidation catalytic processes on the surface of BiVO<sub>4</sub>

and the rate of surface charge recombination. The deuterium kinetic isotope effects (KIEs) can reflect the proton transfer kinetic information on water oxidation reactions and help us to interpret the rate determine step (RDS) of the catalytic process.<sup>[28]</sup> The KIEs(H/D) can be defined as Eq. S7, the current densities in water and deuterated water electrolytes were contrasted at the same overpotential according to Eq. S8–Eq. S10 for KIEs(H/D) measurements in this work.<sup>[29]</sup>

As shown in Figure 5b, the value of KIEs of Co@CB[5]/ITO electrode was larger than 2, indicating a primary KIEs for which O–H bond cleavage is involved in the RDS of electro-driven water oxidation for Co@CB[5], corresponding to the water nucleophilic attack mechanisms.<sup>[28]</sup> When the Co@CB[5] was anchored on the surface of BiVO<sub>4</sub>, the value of KIEs for Co@CB[5]/BiVO<sub>4</sub> photoanode was around 1.0 with the applied bias increasing, indicating the O–H bond cleavage is not involved in the RDS for light driven water oxidation by Co@CB[5]/BiVO<sub>4</sub> photoanode (Figure 5c). In contrast, the value of KIEs for bare BiVO<sub>4</sub> photoanode was around 1.5 (Figure 5d), suggesting that the proton transfer process was involved in the RDS of the light-driven water oxidation process for bare BiVO<sub>4</sub>. Thereby, the immobilization of Co@CB[5] on the surface of BiVO<sub>4</sub> could greatly accelerate the proton transfer processes (water oxidation) and shift the RDS of BiVO<sub>4</sub> photoanode to a non proton transfer involved process. Thence, Co@CB[5] indeed played an important role in the light-driven catalytic water oxidation processes in this Co@CB[5]/BiVO<sub>4</sub> supramolecular assembly photoanode.

It has been known that a co-catalyst can serve as passivation layer to improve charge-separation and charge

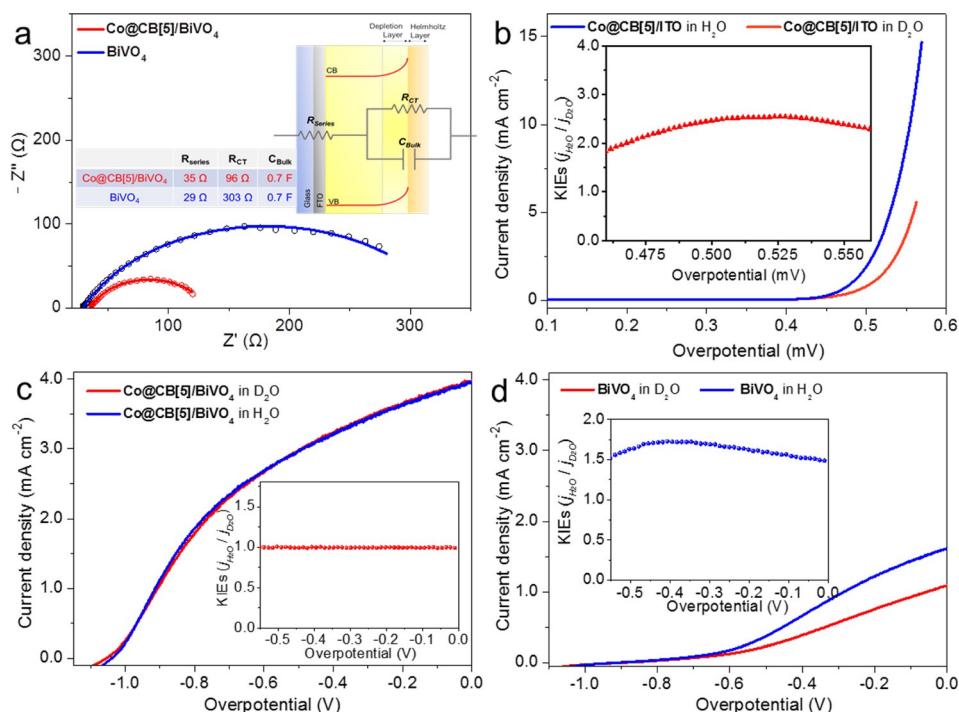


**Figure 5.** a) EIS of BiVO<sub>4</sub> and Co@CB[5]/BiVO<sub>4</sub> photoanodes measured under 0.6 V vs. RHE and AM 1.5G (100 mWcm<sup>-2</sup>) in 1.0 M borate buffer (pH 9.2). b) LSV curves of Co@CB[5]/ITO in anhydrous sodium borate H<sub>2</sub>O and D<sub>2</sub>O solutions, the inset exhibits the KIEs against potential. c), d) LSV curves of Co@CB[5]/BiVO<sub>4</sub> (c) and BiVO<sub>4</sub> (d) in anhydrous sodium borate H<sub>2</sub>O and D<sub>2</sub>O solutions under light irradiation, the inset exhibits the corresponding KIEs against potential.

transfer processes across semiconductor-liquid interfaces.<sup>[30]</sup> For example, the modification of CoPi on the surface of semiconductors can improve the performances of photoanodes, which primarily caused by reducing the surface charge recombination (passivation layer), rather than improving the catalytic ability (charge transfer kinetics).<sup>[31,32]</sup> Similar phenomena have also been observed in other systems, such as a thin layer of  $\text{CoFeO}_x$  modified hematite and  $\text{BiFeO}_3$  passivated  $\text{BiVO}_4$  photoanodes.<sup>[33,34]</sup> Converse systems have also been reported, for instance, thin layers of  $\text{FeOOH}$  can enhance the performance of  $\text{BiVO}_4$  for water oxidation, for which the performance was improved primarily owing to the improvement of charge transfer, rather than suppressing the surface charge recombination.<sup>11</sup> Molecular-based catalysts can also improve the light-driven water oxidation ability of n-type semiconductors, such as Co-salophen complexes and  $\text{Ni}_4\text{O}_4$  cubane have been reported as the co-catalyst for  $\text{BiVO}_4$ ,<sup>[35,36]</sup> in these cases, molecular catalysts can accelerate the water oxidation reaction as OER catalysts, meanwhile, reduce the surface charge recombination.

Our results confirmed that  $\text{Co@CB[5]}$  can effectively promote  $\text{BiVO}_4$  for light-driven water oxidation by serving as a good OER catalyst, however, it is necessary to further confirm whether  $\text{Co@CB[5]}$  on the semiconductor inhibited surface charge recombination by acting as a surface passivation layer. The charge transfer and surface recombination kinetics were quantified by intensity modulated photocurrent spectroscopy (IMPS) to understand the real role of  $\text{Co@CB[5]}$  on the  $\text{BiVO}_4$ . Figure 6a and 6b show typical IMPS responses of bare  $\text{BiVO}_4$  and  $\text{Co@CB[5]/BiVO}_4$  photoanodes

in the complex plane. The IMPS spectrum consists of two semicircles in the 4th and 1st quadrants, which correspond to the resistance-capacitance attenuation and the competition between charge transfer and recombination, respectively.<sup>[34]</sup> Accordingly, the frequency of the maximum imaginary corresponds to the sum of the charge transfer ( $k_{\text{trans}}$ ) and charge recombination ( $k_{\text{rec}}$ ) rate constants ( $k_{\text{trans}} + k_{\text{rec}} = 2\pi f_{\text{max}}$ ). The low frequency intercept in the normalized form, at which the imaginary part is equal to 0, corresponds to a charge transfer efficiency of  $k_{\text{trans}}/(k_{\text{trans}} + k_{\text{rec}})$ .<sup>[37]</sup> The key parameters  $k_{\text{rec}}$  and  $k_{\text{trans}}$  are therefore readily accessible.

Moreover, the upper semicircle of the  $\text{BiVO}_4$  photoanode did not change notably as the applied potential was increased, the value of  $k_{\text{rec}}$  remained nearly constant with increasing potential for bare  $\text{BiVO}_4$  (Figure 6c), indicating that a high charge recombination exists for the  $\text{BiVO}_4$  photoanode over a wide potential range. By contrast, the upper semicircle of the  $\text{Co@CB[5]/BiVO}_4$  photoanode became smaller as the applied potential increased. Notably,  $k_{\text{rec}}$  was suppressed by a factor of 6.5–30 over the entire potential range after decoration of  $\text{Co@CB[5]}$ . For instance, at 0.6 V vs. RHE (the max point of ABPEs), the value of  $k_{\text{rec}}$  was  $3.5 \text{ s}^{-1}$  for bare  $\text{BiVO}_4$ , which is 6.5 times as large as that of  $\text{Co@CB[5]/BiVO}_4$  ( $0.54 \text{ s}^{-1}$ ). At higher potentials, this factor increased to 30 at 0.8 V vs. RHE. These results suggest that the charge recombination was markedly suppressed by the  $\text{Co@CB[5]}$ . Figure 6d shows that the  $k_{\text{trans}}$  of  $\text{Co@CB[5]/BiVO}_4$  surpassed that of  $\text{BiVO}_4$  at all potentials. Particularly, at a potential of 0.6 V vs. RHE (the max point of ABPEs), the  $k_{\text{trans}}$  of  $\text{Co@CB[5]/BiVO}_4$  was more than 4 times as great as that of

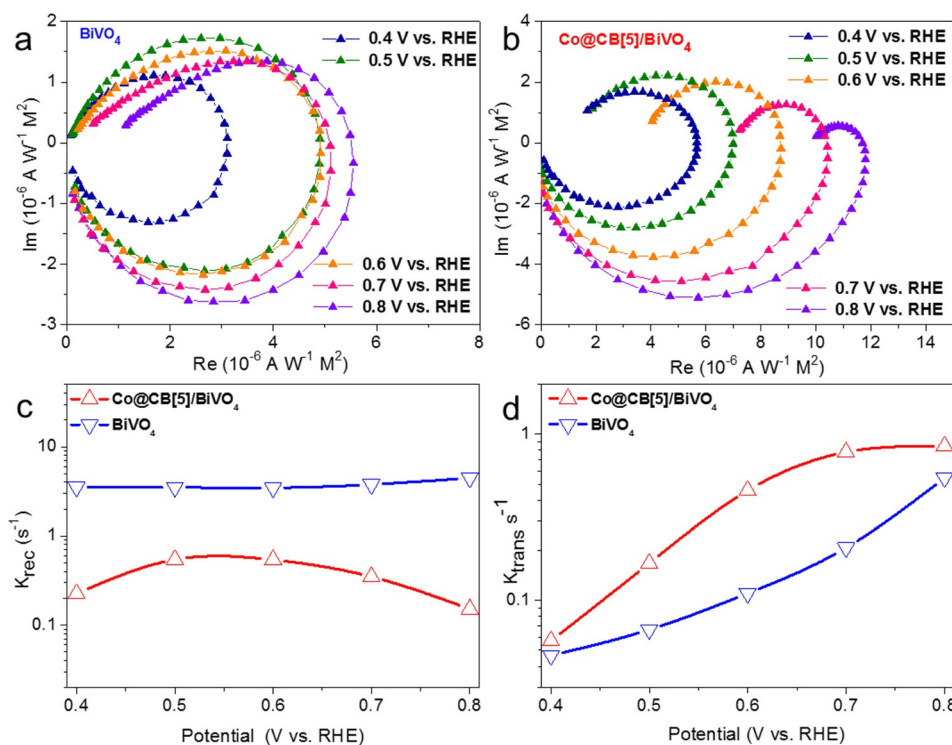
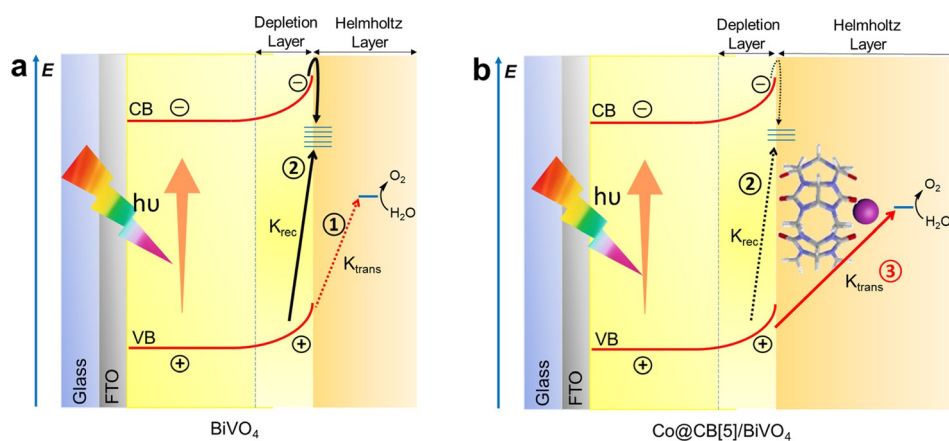


**Figure 6.** a) IMPS spectra of  $\text{BiVO}_4$  photoanode at various potentials. b) IMPS spectra of  $\text{Co@CB[5]/BiVO}_4$  photoanode at various potentials. c) Rate constant for charge recombination,  $k_{\text{rec}}$  extracted from IMPS spectra. d) Rate constant for charge transfer,  $k_{\text{trans}}$  extracted from IMPS spectra.



**Scheme 2.** Simplified elementary processes in a) bare BiVO<sub>4</sub> and b) Co@CB[5]/BiVO<sub>4</sub> photoanode. The movement of holes that were generated from photo-induced charge separation have three pathways at the semiconductor-electrolyte interface (solid lines: majority events; dotted lines: minority events): 1) direct water oxidation with low  $k_{\text{trans}}$ , 2) surface charge recombination, and 3) charge transfer via Co@CB[5] with high  $k_{\text{trans}}$ .

BiVO<sub>4</sub>. The charge transfer efficiency, defined as  $k_{\text{trans}}/(k_{\text{trans}} + k_{\text{rec}})$ , showed the same trend as the value determined by  $J_{\text{water}}/J_{\text{sulfite}}$ , indicating the reliability of our measurements (Figure S37). The ratio of  $k_{\text{rec}}/k_{\text{trans}}$  was positively proportional to the semicircle in 1st quadrant and a small value indicated faster charge transfer than charge recombination.<sup>[34]</sup> These results demonstrate that Co@CB[5] behaves as a molecular catalyst, which is in contrast to the mere passivation action of heterogeneous catalysts as reported,<sup>[31–34]</sup> Co@CB[5] not only accelerates the water oxidation reaction as a good OER catalyst for BiVO<sub>4</sub>, but also reduces the surface charge recombination.

Based on the OER kinetics analyzed above, the function of Co@CB[5] on BiVO<sub>4</sub> was summarized and shown in Scheme 2. For the bare BiVO<sub>4</sub>, the photo-generated holes can be directly consumed for water oxidation (pathway 1), or recombined with electrons that trapped by surface state (pathway 2). Due to the low intrinsic OER catalytic activity of BiVO<sub>4</sub>, the injection of holes to electrolyte was limited by the proton transfer involved water oxidation reaction, leading to a primary KIEs for bare BiVO<sub>4</sub>. When Co@CB[5] was immobilized on the surface of BiVO<sub>4</sub>, owing to the high OER catalytic activity of Co@CB[5], the photo-generated holes could be effectively transferred and consumed for water oxidation (pathway 3); meanwhile, due to the faster consumption of holes, the photo-generated electrons will have less chance to recombine with photo-generated holes at the surface of BiVO<sub>4</sub>, leading to the higher charge transfer efficiency of Co@CB[5]/BiVO<sub>4</sub> in comparison to that of the bare BiVO<sub>4</sub>.

## Conclusion

A host–guest supramolecular complex Co@CB[5] as a molecular water oxidation catalyst was successfully immobilized on porous ITO and BiVO<sub>4</sub> substrates. This supramolecular catalyst Co@CB[5] showed a high activity for electrochemical water oxidation when immobilized on a porous ITO substrate, the fabricated Co@CB[5]/ITO electrode

exhibited a TOF of 9.9 s<sup>−1</sup> at an overpotential of 550 mV in a pH 9.2 borate buffer with good stability. When Co@CB[5] was immobilized on the surface of the porous BiVO<sub>4</sub> n-type semiconductor, the integrated photoanode Co@CB[5]/BiVO<sub>4</sub> showed an excellent PEC performance with a high photocurrent density of 4.8 mA cm<sup>−2</sup> at 1.23 V (vs. RHE) under 100 mW cm<sup>−2</sup> (AM 1.5) light illumination. KIEs and IMPS results confirmed that Co@CB[5] serves as a supramolecular water oxidation catalyst which can effectively accelerate surface charge transfer. Furthermore, the surface charge recombination of BiVO<sub>4</sub> can also be suppressed by this host–guest supramolecular complex. The host–guest complex Co@CB[5] shows a remarkable performance for electrochemical and PEC water oxidation, which can open new opportunities for the development of supramolecular complexes as catalysts for not only efficient water oxidation, but may also for other catalytic reactions.

## Acknowledgements

This work was financially supported by the Fundamental Research Funds for the Central Universities (DUT19LK16), the National Natural Science Foundation of China (Grant No. 21120102036), the Swedish Research Council (2017-00935), and the K & A Wallenberg Foundation (KAW 2016.0072).

## Conflict of interest

The authors declare no conflict of interest.

**Keywords:** electrocatalysis · host–guest complexes · PEC cells · supramolecular catalysts · water splitting

[1] T. R. Cook, D. K. Dogutan, S. Y. Reece, Y. Surendranath, T. S. Teets, D. G. Nocera, *Chem. Rev.* **2010**, *110*, 6474–6502.

[2] B. Zhang, L. Wang, Y. Zhang, Y. Ding, Y. Bi, *Angew. Chem. Int. Ed.* **2018**, *57*, 2248–2252; *Angew. Chem.* **2018**, *130*, 2270–2274.

- [3] M. Wang, Y. Yang, J. Shen, J. Jiang, L. Sun, *Sustainable Energy Fuels* **2017**, *1*, 1641–1663.
- [4] S. Anantharaj, S. R. Ede, K. Sakthikumar, K. Karthick, S. Mishra, S. Kundu, *ACS Catal.* **2016**, *6*, 8069–8097.
- [5] Y. Park, K. J. McDonald, K.-S. Choi, *Chem. Soc. Rev.* **2013**, *42*, 2321–2337.
- [6] X. Chang, T. Wang, P. Zhang, J. Zhang, A. Li, J. Gong, *J. Am. Chem. Soc.* **2015**, *137*, 8356–8359.
- [7] T. W. Kim, K.-S. Choi, *Science* **2014**, *343*, 990–994.
- [8] F. Yu, F. Li, T. Yao, J. Du, Y. Liang, Y. Wang, H. Han, L. Sun, *ACS Catal.* **2017**, *7*, 1868–1874.
- [9] S. K. Pilli, T. E. Furtak, L. D. Brown, T. G. Deutsch, J. A. Turner, A. M. Herring, *Energy Environ. Sci.* **2011**, *4*, 5028–5034.
- [10] S. K. Choi, W. Choi, H. Park, *Phys. Chem. Chem. Phys.* **2013**, *15*, 6499–6507.
- [11] K. Dang, X. Chang, T. Wang, J. Gong, *Nanoscale* **2017**, *9*, 16133–16137.
- [12] Y. Wang, F. Li, X. Zhou, F. Yu, J. Du, L. Bai, L. Sun, *Angew. Chem. Int. Ed.* **2017**, *56*, 6911–6915; *Angew. Chem.* **2017**, *129*, 7015–7019.
- [13] S. Ye, C. Ding, R. Chen, F. Fan, P. Fu, H. Yin, X. Wang, Z. Wang, P. Du, C. Li, *J. Am. Chem. Soc.* **2018**, *140*, 3250–3256.
- [14] X.-L. Ni, X. Xiao, H. Cong, L.-L. Liang, K. Cheng, X.-J. Cheng, N.-N. Ji, Q.-J. Zhu, S.-F. Xue, Z. Tao, *Chem. Soc. Rev.* **2013**, *42*, 9480–9508.
- [15] T. V. Mitkina, N. F. Zakharchuk, D. Y. Naumov, O. A. Gerasko, D. Fenske, V. P. Fedin, *Inorg. Chem.* **2008**, *47*, 6748–6755.
- [16] M. Freitag, E. Galoppini, *Langmuir* **2010**, *26*, 8262–8269.
- [17] M. Porel, A. Klimczak, M. Freitag, E. Galoppini, V. Ramamurthy, *Langmuir* **2012**, *28*, 3355–3359.
- [18] J. Lagona, P. Mukhopadhyay, S. Chakrabarti, L. Isaacs, *Angew. Chem. Int. Ed.* **2005**, *44*, 4844–4870; *Angew. Chem.* **2005**, *117*, 4922–4949.
- [19] D. K. Lee, K.-S. Choi, *Nat. Energy* **2018**, *3*, 53–60.
- [20] H. You, D. Wu, Z.-n. Chen, F. Sun, H. Zhang, Z. Chen, M. Cao, W. Zhuang, R. Cao, *ACS Energy Lett.* **2019**, *4*, 1301–1307.
- [21] H. Woo, E. Kim, J.-H. Kim, S.-W. Yun, J. C. Park, Y.-T. Kim, K. H. Park, *Sci. Rep.* **2017**, *7*, 3851.
- [22] P. T. Babar, A. C. Lokhande, B. S. Pawar, M. G. Gang, E. Jo, C. Go, M. P. Suryawanshi, S. M. Pawar, J. H. Kim, *Appl. Surf. Sci.* **2018**, *427*, 253–259.
- [23] D. Zhao, Z. Chen, W. Yang, S. Liu, X. Zhang, Y. Yu, W.-C. Cheong, L. Zheng, F. Ren, G. Ying, X. Cao, D. Wang, Q. Peng, G. Wang, C. Chen, *J. Am. Chem. Soc.* **2019**, *141*, 4086–4093.
- [24] L. Tong, M. Gothelid, L. Sun, *Chem. Commun.* **2012**, *48*, 10025–10027.
- [25] J. Wang, L. Gan, W. Zhang, Y. Peng, H. Yu, Q. Yan, X. Xia, X. Wang, *Sci. Adv.* **2018**, *4* eaap7970.
- [26] T. W. Kim, Y. Ping, G. A. Galli, K.-S. Choi, *Nat. Commun.* **2015**, *6*, 8769.
- [27] J. K. Kim, Y. Cho, M. J. Jeong, B. Levy-Wendt, D. Shin, Y. Yi, D. H. Wang, X. Zheng, J. H. Park, *ChemSusChem* **2018**, *11*, 933–940.
- [28] F. Li, K. Fan, L. Wang, Q. Daniel, L. Duan, L. Sun, *ACS Catal.* **2015**, *5*, 3786–3790.
- [29] W. Li, F. Li, H. Yang, X. Wu, P. Zhang, Y. Shan, L. Sun, *Nat. Commun.* **2019**, *10*, 5074.
- [30] R. Liu, Z. Zheng, J. Spurgeon, X. Yang, *Energy Environ. Sci.* **2014**, *7*, 2504–2517.
- [31] C. Zachäus, F. F. Abdi, L. M. Peter, R. van de Krol, *Chem. Sci.* **2017**, *8*, 3712–3719.
- [32] Y. Ma, A. Kafizas, S. R. Pendlebury, F. Le Formal, J. R. Durrant, *Adv. Funct. Mater.* **2016**, *26*, 4951–4960.
- [33] J. Zhang, R. García-Rodríguez, P. Cameron, S. Eslava, *Energy Environ. Sci.* **2018**, *11*, 2972–2984.
- [34] J. Xie, C. Guo, P. Yang, X. Wang, D. Liu, C. M. Li, *Nano Energy* **2017**, *31*, 28–36.
- [35] Y. Liu, Y. Jiang, F. Li, F. Yu, W. Jiang, L. Xia, *J. Mater. Chem. A* **2018**, *6*, 10761–10768.
- [36] B. Gao, T. Wang, X. Fan, H. Gong, P. Li, Y. Feng, X. Huang, J. He, J. Ye, *J. Mater. Chem. A* **2019**, *7*, 278–288.
- [37] F. Li, Y. Li, Q. Zhuo, D. Zhou, Y. Zhao, Z. Zhao, X. Wu, Y. Shan, L. Sun, *ACS Appl. Mater. Interfaces* **2020**, *12*, 11479–11488.

Manuscript received: August 17, 2020

Revised manuscript received: September 25, 2020

Accepted manuscript online: October 13, 2020

Version of record online: November 24, 2020